Effects of Dynamic Vegetation on Global Climate Simulation Using the NCEP GFS and SSiB4/TRIFFID

Zhengqiu ZHANG[1], Yongkang XUE[2], Panmao ZHAI[1*], and Huiping DENG[3]

1 *Chinese Academy of Meteorological Sciences*, *China Meteorological Administration*, *Beijing* 100081, *China*
2 *University of California*, *Los Angeles*, *CA* 90095, *USA*
3 *Liaocheng University*, *Liaocheng* 252059, *China*

ABSTRACT

Two global experiments were carried out to investigate the effects of dynamic vegetation processes on numerical climate simulations from 1948 to 2008. The NCEP Global Forecast System (GFS) was coupled with a biophysical model, the Simplified Simple Biosphere Model (SSiB) version 2 (GFS/SSiB2), and it was also coupled with a biophysical and dynamic vegetation model, SSiB version 4/Top-down Representation of Interactive Foliage and Flora Including Dynamics (TRIFFID) (GFS/SSiB4/TRIFFID). The effects of dynamic vegetation processes on the simulation of precipitation, near-surface temperature, and the surface energy budget were identified on monthly and annual scales by assessing the GFS/SSiB4/TRIFFID and GFS/SSiB2 results against the satellite-derived leaf area index (LAI) and albedo and the observed land surface temperature and precipitation. The results show that compared with the GFS/SSiB2 model, the temporal correlation coefficients between the globally averaged monthly simulated LAI and the Global Inventory Monitoring and Modeling System (GIMMS)/Global Land Surface Satellite (GLASS) LAI in the GFS/SSiB4/TRIFFID simulation increased from 0.31/0.29 (SSiB2) to 0.47/0.46 (SSiB4). The correlation coefficients between the simulated and observed monthly mean near-surface air temperature increased from 0.50 (Africa), 0.35 (Southeast Asia), and 0.39 (South America) to 0.56, 0.41, and 0.44, respectively. The correlation coefficients between the simulated and observed monthly mean precipitation increased from 0.19 (Africa), 0.22 (South Asia), and 0.22 (East Asia) to 0.25, 0.27, and 0.28, respectively. The greatest improvement occurred over arid and semiarid areas. The spatiotemporal variability and changes in vegetation and ground surface albedo modeled by the GFS with a dynamic vegetation model were more consistent with the observations. The dynamic vegetation processes contributed to the surface energy and water balance and in turn, improved the annual variations in the simulated regional temperature and precipitation. The dynamic vegetation processes had the greatest influence on the spatiotemporal changes in the latent heat flux. This study shows that dynamic vegetation processes in earth system models significantly improve simulations of the climate mean status.

Key words: NCEP Global Forecast System (GFS), Simplified Simple Biosphere Model version 4/Top-down Representation of Interactive Foliage and Flora Including Dynamics (SSiB4/TRIFFID), global climate simulation, effects of dynamic vegetation

---

1. Introduction

Vegetation has a close relationship with both precipitation and temperature (Wang et al., 2008; Zhong et al., 2010; Cao et al., 2011; Claussen et al., 2013) and can affect climate processes and climate variability (Wang et al., 2004; Crucifix et al., 2005; Zeng et al., 2008; Zhi et al., 2009; Zeng et al., 2017). Numerical studies have been carried out to identify vegetation–climate relationships. For example, by using the NCEP Global Forecast System (GFS), the effects and mechanisms of the biophysical processes of vegetation on summer precipitation have been explored on both global and continental scales (Xue et al., 2004, 2010; Xue, 2006). These results

showed that the feedbacks between vegetation and the atmosphere have an important role in the global and regional water cycle, particularly in monsoon regions and some of the larger continents, such as North America. Although differences between the dry and wet seasons can be identified in these areas, the developmental processes of monsoons, such as the northward jump in early stages of the East Asian monsoon, cannot be reproduced if the biophysical processes of vegetation are not included in the GFS.

The importance of vegetation to climate, especially their two-way interactions, has been identified in a number of studies (Levis and Bonan, 2004; Delire et al., 2011; Wang et al., 2011; Wu et al., 2016; Yu et al., 2016; Shi et al., 2018). Using a prognostic leaf area index (LAI) parameterization, Levis and Bonan (2004) found that the observed reduction in the springtime warming trend over the Northern Hemisphere was only simulated when photosynthesis, stomatal conductance, and leaf emergence were synchronized with the surface climate. Zeng et al. (1999) found that dynamic vegetation processes could enhance the low-frequency variability of rainfall in the Sahel region. Wang et al. (2011) presented evidence from a numerical model that vegetation dynamics might have contributed to the observed low-frequency variability of precipitation in the Amazon basin. Delire et al. (2004) showed that this enhancement of the low-frequency variability of precipitation by vegetation dynamics was most likely to occur in the transition zone between dry and wet climates.

The characteristics of this feedback have been investigated. Delire et al. (2011) summarized their modeled vegetation–atmosphere feedback as positive temperature feedback at mid to high latitudes and negative feedback in semiarid regions, as well as positive precipitation feedback in semiarid regions. Using a regional earth system model coupled with an interactive vegetation–atmosphere model in the representative concentration pathway (RCP) 8.5 future climate scenario, Wu et al. (2016) found that vegetation-mediated feedbacks in Africa were generally negative with respect to temperature and positive with respect to precipitation, enhancing the reduction in rainfall over the rainforest areas (Wu et al., 2016). In another African study, Yu et al. (2016) used a regional climate model with dynamic vegetation processes to investigate the role of vegetation feedback in future climate change in West Africa. A high sensitivity of climate projection to dynamic vegetation feedback was found mainly in the semiarid areas of West Africa, but there was little signal in the wet tropics (Yu et al., 2016).

Using the Regional Climate Model (RegCM) coupled

with the Community Land Model (CLM), including modules of carbon–nitrogen cycling (CN) and vegetation dynamics (DV), Shi et al. (2018) evaluated the performance of the model with different capacities to represent vegetation processes in simulating the present day climate over China. They found that relative to RegCM-CLM, both RegCM-CLM-CN and RegCM-CLM-CN-DV performed better in simulating the interannual variability of temperature and the spatial distribution of mean precipitation, but produced larger biases in the mean temperature field as a result of an overestimation of the LAI and/or an underestimation of the vegetation cover (Shi et al., 2018).

To assess the ability of current dynamic vegetation models to produce the observed vegetation dynamics and to contribute to bias in climate simulations, an offline study using the Simplified Simple Biosphere Model version 4 (SSiB4)/Top-down Representation of Interactive Foliage and Flora Including Dynamics (TRIFFID) model was conducted (Zhang et al., 2015; Liu et al., 2019). Meteorological forcing was used to drive the SSiB4/TRIFFID simulation without feedback to the atmosphere in order to identify the major factors underlying the connections between vegetation dynamics and climate variability. The spatial distribution and temporal variability of vegetation on seasonal to decadal scales were investigated over North America (Zhang et al., 2015). The SSiB4/TRIFFID simulation reproduced the main features of North America as well as the global distribution of dominant vegetation types, the vegetation fraction, and the LAI, including its seasonal, interannual, and decadal variabilities (Zhang et al., 2015; Liu et al., 2019). However, an investigation of the fully coupled two-way interaction is required to more comprehensively understand the effects of dynamic vegetation processes on climate modeling.

By taking advantage of the improved SSiB4/TRIFFID model, the SSiB4/TRIFFID and SSiB2 models were coupled with the GFS to investigate vegetation–atmosphere feedback and the effects of dynamic vegetation processes on global climate simulations. Two experiments were conducted globally by integrating the GFS/SSiB4/TRIFFID and GFS/SSiB2 simulations from 1948 to 2008. The coupled GFS/SSiB4/TRIFFID model includes dynamic vegetation processes, whereas the other model does not include a dynamic vegetation component.

By assessing the GFS/SSiB4/TRIFFID and GFS/SSiB2 results against the satellite-derived LAI and albedo, as well as the observed land surface temperature and precipitation, the effects of dynamic vegetation processes on the simulation of precipitation, near-surface temperature,

and the surface energy budget were identified on monthly and annual scales.

2. Model and methods

2.1 SSiB4/TRIFFID model

TRIFFID has been widely used in vegetation–climate interaction studies (Cox et al., 2000; Harper et al., 2016). In TRIFFID, the vegetation coverage, LAI, and canopy height of each plant functional type (PFT) are updated based on the carbon balance. The changes to vegetation cover are driven by the assimilation, distribution, and accumulation of carbon, and competition between PFTs. For a specific PFT, the carbon density (C_v) calculation is based on the carbon balance and competition with other PFTs:

$$\frac{dC_v}{dt} = (1 - \lambda)\Pi - \Lambda_l, \tag{1}$$

where Π is the net primary productivity, λ is the portion of carbon used for PFT fraction expansion, and Λ_l is the local litterfall rate.

The fractional coverage (v) for each PFT is calculated by:

$$C_v \frac{dv}{dt} = \lambda \Pi v_* \left(1 - \sum_j C_{ij} v_j\right) - \gamma_v v_* C_v, \tag{2}$$

where $v_* = \max\{v, 0.01\}$, γ_v is the large scale disturbance rate, v_j is the coverage of plant type j ($j = 1$–6), and C_{ij} is a competition coefficient between the ith plant type and the jth plant type, which is determined by the competition equation based on the Lotka–Volterra approach.

The original TRIFFID model defines the pattern of vegetation at a grid point as being composed of five PFTs. A new type (tundra shrub) has been added to the TRIFFID model to simulate the vegetation in cold regions. SSiB4/TRIFFID therefore categorizes global vegetation into six major PFTs: broadleaf forest, coniferous forest, C3 grasses, C4 plants, shrubs, and tundra shrubs (Cox, 2001; Xue, 2006; Zhang et al., 2015).

The SSiB model has been widely used in global and regional climate studies (Xue et al., 1991). It provides calculations for runoff, radiation, momentum, sensible heat flux, and latent heat flux. The offline version of SSiB has been tested by using data from different sites and different types of vegetation around the world (Xue et al., 2001). A photosynthesis model has been implemented into SSiB to calculate carbon assimilation, forming SSiB2 (Zhan et al., 2003). To investigate the interactions between vegetation and climate, the TRIFFID model (Cox, 2001) was coupled to SSiB4 (SSiB4/TRIFFID)

(Xue, 2006). A large number of tests have been conducted at sites and on regional and global scales to evaluate the capabilities of the SSiB4/TRIFFID model (Xue, 2006; Zhang et al., 2015; Liu et al., 2019; Liu and Xue, 2020). In the coupled SSiB4/TRIFFID model, SSiB4 provides estimates of the net plant photosynthesis assimilation rate, autotrophic respiration, and other surface conditions (e.g., soil moisture and canopy temperature) for TRIFFID. TRIFFID calculates the vegetation dynamics, including the relevant land surface characteristics of the vegetation cover and structure (e.g., plant height and LAI) for SSiB4.

2.2 Dataset and experimental design

2.2.1 Dataset
2.2.1.1 Satellite-derived LAI data

Two widely used LAI products were used as a reference to validate the simulation ability of the GFS/SSiB4/TRIFFID model: the Global Inventory Monitoring and Modeling System (GIMMS) Boston University (GIMMSBU) LAI with a spatial resolution of 0.25° and a temporal coverage from 1982 to 2011 (Pinzon et al., 2005; Zhu et al., 2013), and the Global Land Surface Satellite (GLASS) LAI with a spatial resolution of 0.5° and a temporal coverage from 1981 to 2012 (Xiao et al., 2016). These two global biophysical land surface datasets are processed as monthly averages.

The GLASS LAI product is generated from time series of the Moderate Resolution Imaging Spectroradiometer (MODIS) and Advanced Very High Resolution Radiometer (AVHRR) reflectance data using a general regression neural network method (Xiao et al., 2016). The GIMMS normalized difference vegetation index product uses the original raw AVHRR rather than the Pathfinder corrected bands. Because these two datasets provide invaluable surface vegetation information and a measure of the uncertainty in the satellite products, both the LAIs are used to evaluate the model simulations.

2.2.1.2 GLC2000

The global land cover database for the year 2000 (GLC2000) was used to compare the vegetation types. GLC2000 contains two levels of land cover information: detailed, regionally optimized land cover legends for each continent and a less thematically detailed global legend that harmonizes the regional legends into one consistent product. The land cover maps are all based on daily data from the VEGETATION sensor onboard the SPOT 4 satellite, although mapping of some regions involved the use of data from other earth-observing sensors to resolve specific issues (Bartholomé and Belward, 2005). This dataset has a spatial resolution of 1 km and

22 classifications of vegetation types. For comparison with the vegetation types produced by the model, the GLC2000 Global Product was downloaded and processed at spatial resolution T62 (about 2.0°) by statistically accounting for the number of vegetation types in GLC2000 in the T62 grid and taking a large number of the same types of vegetation as the dominant vegetation type. To better compare the modeled vegetation types with the observations, the vegetation types of GLC2000 were reclassified into 10 types (Table 1).

2.2.1.3 MODIS albedo data

We used the MODIS albedo products. These data products are currently available at 500-m resolution in the sinusoidal projection and 0.05° in the latitude/longitude projection for every 8 days since early 2000 (Schaaf et al., 2002; Gao et al., 2005). The MCD43C product provides both the black sky albedo (BSA) and the white sky albedo (WSA). The BSA is a function of the solar zenith angle and is defined as the albedo without the diffuse radiation component. The WSA is independent of the solar zenith angle and is defined as the albedo without the direct radiation component. The all-sky albedo is calculated by combining the BSA and WSA (Lucht et al., 2000):

$$\alpha = (1 - f_{\text{dif}})\alpha_{\text{bs}} + f_{\text{dif}}\alpha_{\text{ws}}, \qquad (3)$$

where α is the all-sky albedo, f_{dif} is the diffuse skylight fraction, and α_{bs} and α_{ws} are the BSA and WSA, respectively. In previous papers, the diffuse skylight fraction has not been taken into consideration when calculating the all-sky albedo (Zhang et al., 2010). He et al. (2014),

however, used the monthly diffuse and direct downward radiation from the NCEP reanalysis dataset to calculate the diffuse skylight fraction and found that the diffuse skylight fraction varied over both time and space. Qiu et al. (2016) used monthly diffuse and direct downward radiation data from the NCEP dataset to calculate the diffuse skylight fraction. We used the MODIS albedo data from Qiu et al. (2016).

2.2.1.4 Near-surface air temperature and precipitation

The Global Historical Climatology Network and Climate Anomaly Monitoring System (GHCN_CAMS) Gridded 2 m Temperature (Land) model was used to compare the difference in air temperature simulated by the GFS. This dataset consists of high-resolution analyzed global land surface temperatures from 1948 to near the present day, with a spatial coverage of 0.5° latitude × 0.5° longitude on a global grid (360 × 720) (Fan and van den Dool, 2008). The Climate Prediction Center Merged Analysis of Precipitation (CMAP) rain dataset was also used. This provides monthly and pentad global gridded precipitation means and has a temporal coverage from 1979 to the present day, with a spatial coverage of 2.5° latitude × 2.5° longitude on a global grid (144 × 72) (Xie and Arkin, 1997).

2.2.2 *Experimental design*

We used the NCEP GFS to investigate the mechanism of the interaction between dynamic vegetation processes and climate. The SSiB2 and SSiB4/TRIFFID models were incorporated into the NCEP GFS (the NCEP GFS/SSiB2 and the NCEP GFS/SSiB4/TRIFFID). Using the GFS/SSiB2 and GFS/SSiB4/TRIFFID models, two

Table 1. Comparisons of different land cover classification schemes

SSiB4/TRIFFID		GLC2000	
Class	Description	Class	Description
		1	Tree cover, broadleaf, evergreen
1	Broadleaf trees	2	Tree cover, broadleaf, deciduous, closed
		3	Tree cover, broadleaf, deciduous, open
2	Needleleaf trees	4	Tree cover, needleleaf, evergreen
		5	Tree cover, needleleaf, deciduous
3	C3 grasses	13	Herbaceous cover, closed–open
4	C4 plants	15	Regularly flooded shrub and/or herbaceous cover
5	Shrubs	11	Shrub cover, closed–open, evergreen
		14	Sparse herbaceous or sparse shrub cover
6	Tundra shrubs	12	Shrub cover, closed–open, deciduous
7	Bare land	19	Bare areas
		22	Artificial surfaces and associated areas
8	Crops	16	Cultivated and managed areas
		6	Tree cover, mixed-leaf type
		7	Tree cover, regularly flooded, fresh water
		8	Tree cover, regularly flooded, saline water
9	Mixed forest	9	Mosaic: tree cover/other natural vegetation
		10	Tree cover, burned
		17	Mosaic: cropland/tree cover/other natural vegetation
		18	Mosaic: cropland/shrub and/or grass cover
10	Snow and ice	21	Snow and ice
11	Water	20	Water bodies

simulations were conducted from 1948 to 2008 with the same initial conditions using the NCEP reanalysis dataset, including sea ice, sea temperature, and the land surface conditions. In the simulation, the sea ice and sea temperature were taken as climate averages from the NCEP reanalysis dataset for the same period of the calculation. For the initial land condition, the values of the related variables were taken from the climate averages.

The model spatial resolution is T62 (192 × 94), the time step is 20 min, and the output interval is 6 h. To calculate the correlation coefficients, the data were processed as monthly and yearly means, the same as the satellite-derived data. The spatial resolution was interpolated into T62. The temperature, precipitation, and satellite-derived LAI and albedo were averaged in the grid from a fine resolution and the dominant vegetation types were calculated statistically based on the percentage of vegetation types in the grid.

In GFS/SSiB2, the monthly LAI is specified as an input and is obtained from a Simple Biosphere Model version 2 (SiB2) vegetation parameter table. The table provides the monthly LAI for 13 land cover types and is based on satellite measurements, ground measurements, and literature data (Sellers et al., 1996; Xue et al., 1996). Because the LAI in SSiB2 is based on a table and the LAI is determined based on the land cover type, the LAI dataset itself has no spatial resolution (the spatial resolution is determined by the GFS model grid). The LAI in the table is changed every month (i.e., the temporal resolution is monthly). However, the data have no interannual variation. The results from GFS/SSiB2 were used as a control and compared with the results from the GFS/SSiB4/TRIFFID model to identify the effects of dynamic vegetation processes on the modeled climate.

The LAI is an essential parameter used to monitor global vegetation. Unlike SSiB2, the SSiB4/TRIFFID model has multiple PFTs within each model grid cell. To compare the simulated LAI with GIMMS and GLASS, the total simulated LAI was calculated as the area-weighted average LAI among different PFTs:

$$\mathrm{LAI} = \sum_{i=1}^{6} f_i \mathrm{LAI}_i, \qquad (4)$$

where f_i ($i = 1$–6) is the vegetation fraction for each vegetation type and LAI_i is the LAI for each vegetation type modeled by SSiB4/TRIFFID.

To investigate the effects of dynamic vegetation processes on the regional climate, the globe was divided into eight sub-regions (Xue et al., 2010). The definitions of these sub-regions are given in Table 2 and the corresponding boundaries are shown in Fig. 1. To facilitate the calculations, the regions were divided into rectangular regions. The sub-regions may therefore not be exactly the same as the geographical divisions of the world. In addition to the sub-regions, Fig. 1 also shows the fractional distribution of different vegetation types modeled by SSiB4/TRIFFID; the vegetation fraction is averaged over the last 10 years of the simulation (1998–2008).

Figure 1 shows that after 50 years of model adjustment, the spatial distribution patterns of tundra shrubs, shrubs, and needleleaf trees produced by the SSiB4/TRIFFID model over mid to high latitudes are very similar to those in the GLC2000 map (Latifovic et al., 2002; Mayaux et al., 2004). The distributions of simulated broadleaf trees, C3 grass, and C4 plants are also generally consistent with the published distribution of vegetation (e.g., DeFries and Townshend, 1994; Woodward et al., 2004; MacDonald, 2010).

Figure 2 compares the dominant vegetation types simulated by the GFS/SSiB4/TRIFFID model with those of the GLC2000 model. The GLC2000 model includes croplands, whereas the SSiB4/TRIFFID has only natural vegetation types with no agricultural land. Figure 2 shows that in general, the dominant vegetation types produced by the model agree with the observations. The simulated land cover of broadleaf and needleleaf trees generally agree with the observations, but some differences occur in and around semiarid areas and in some non-forest regions. The SSiB4/TRIFFID model used here did not produce West African shrubland well, but this has been improved in a later version (Liu et al., 2019). The GLC2000 model was unable to show the South African Kalahari and Australian deserts, which were produced by the SSiB4/TRIFFID model. Overall, the SSiB4/TRIFFID model produced a reasonable distribution of the spatial patterns of forest, tundra shrubs, shrubs, and C3 and C4 plants, consistent with the GLC2000 map (Latifovic et al., 2002; Mayaux et al., 2004) and other published distributions of vegetation (e.g., DeFries and Townshend, 1994; Woodward et al., 2004; MacDonald, 2010).

Table 3 compares the percentage of global coverage for each dominant vegetation type among the GLC2000, SSiB4/TRIFFID, and SSiB2 models. Note that the calculation has masked out the areas of types 8 (crops), 9 (mixed forest), 10 (land ice), and 11 (water) of GLC2000 in Table 1. The SSiB4 model has no mixed forest PFT. Table 3 shows that the model biases of C4 plants, shrubs, tundra shrubs, and bare lands simulated by the SSiB4/TRIFFID model are substantially reduced, whereas other types are similar, indicating that the vegetation dynamics improve the ability of the model to simulate the
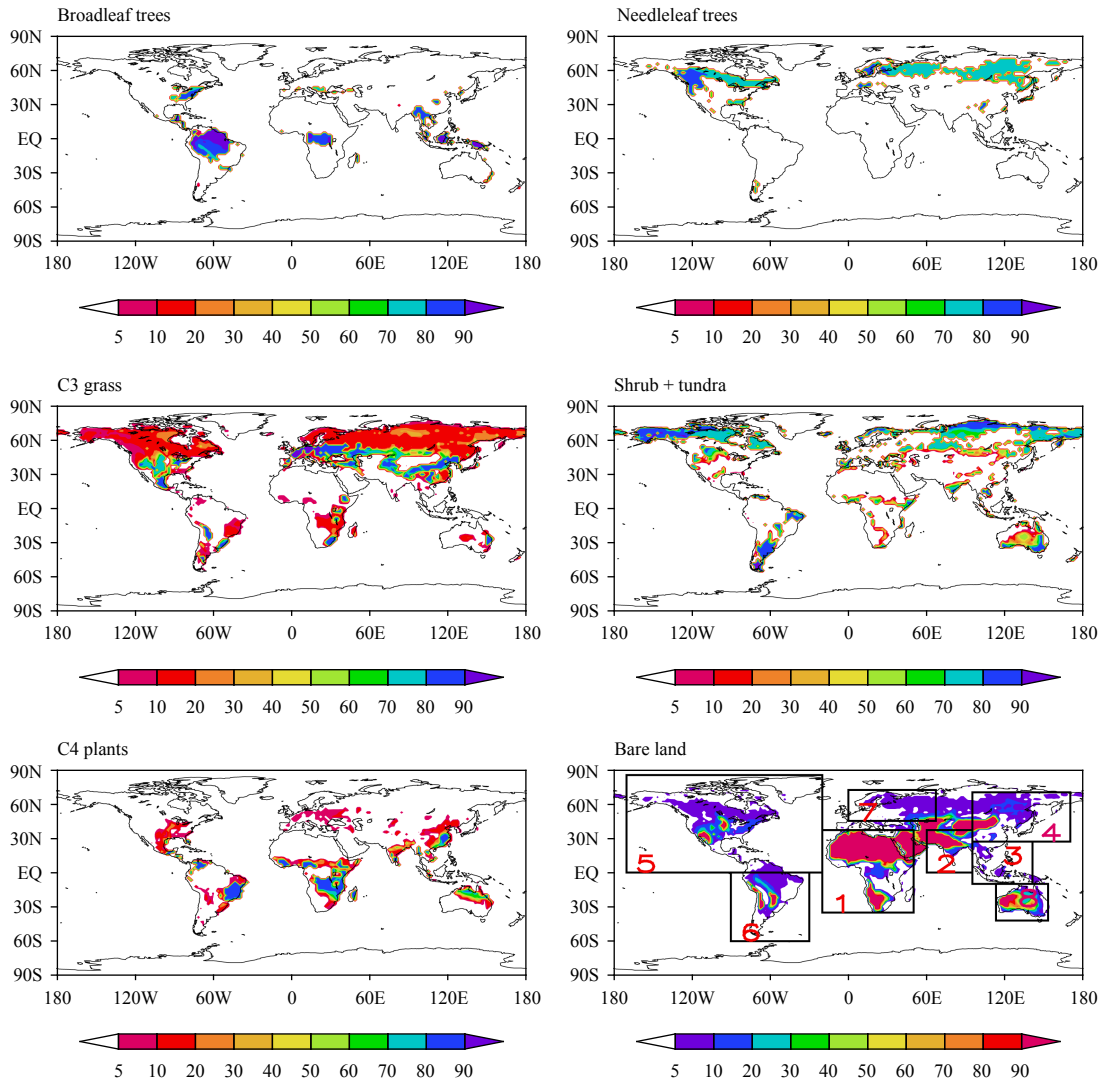
Fig. 1. Simulated vegetation fractions (%) for different PFTs averaged from 1998 to 2008. The black boxes are the eight regions defined in Table 2.

spatial coverage of vegetation types.

3. Comparison of the simulation results with observations

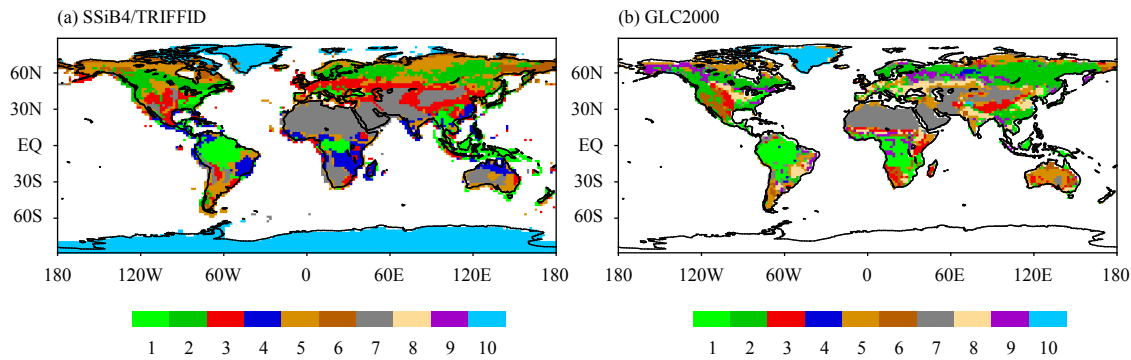### 3.1 *Comparison of the simulated LAI with satellite-derived LAI*

Figures 3 and 4 compare the observed (GIMMS and

Table 2. Domain coordinates of the regions for statistical calculations

Region No.	Name	Longitude	Latitude
1	Africa	20°W–50°E	35°S–37°N
2	South Asia	60°–95°E	0°–37°N
3	Southeast Asia	95°–141°E	10°S–27°N
4	East Asia	95°–170°E	27°–70°N
5	North America	170°–20°W	0°–85°N
6	South America	90°–30°W	60°S–0°
7	Europe	0°–67°E	45°–72°N
8	Australia	113°–153°E	42°–10°S

GLASS) and simulated LAI and the prescribed LAI (Sellers et al., 1996) in the run without dynamic vegetation. The winter (DJF), summer (JJA), and annual (ANN) LAI are averaged over the time period 1982–2008. The differences between two seasons (JJA minus DJF) are also shown to delineate the seasonal variability.

Although the four sets of LAI show some generally similar spatial distribution patterns, there are important differences between SSiB2 and the other simulations. The greatest differences appear in JJA (Figs. 3b$_1$–b$_4$) over the high latitudes of the Northern Hemisphere, Australia, and South and East Asia. The LAIs from the GFS/SSiB4/TRIFFID, GIMMS, and GLASS simulations are generally consistent. The spatial correlation coefficients between the annual averages produced by the GFS/SSiB4/TRIFFID and GIMMS/GLASS simulations are 0.61 and 0.61.

Fig. 2. Comparisons of the dominant vegetation types between the GFS/SSiB4/TRIFFID simulation and satellite products. 1: Broadleaf trees, 2: needleleaf trees, 3: C3 grass, 4: C4 plants (savanna), 5: shrubs, 6: tundra shrubs, 7: bare land, 8: cropland, 9: mixed forest, and 10: ice and snow.

Table 3. Area percentages of dominant vegetation types

Vegetation type	Broadleaf tree	Needleleaf tree	C3 grass	C4 plant	Shrub	Tundra shrub	Bare land
GLC2000	22	26	4	2	27	8	11
SSiB4/TRIFFID	21	20	11	7	23	9	9
SSiB2	21	20	4	16	17	18	4

Table 4 shows the spatial averages of the correlations and standard deviations between the simulated and GLASS monthly mean LAIs from 1982 to 2002 for different regions. The LAI correlations between the SSiB4/TRIFFID and GLASS simulations are relatively higher than those between the SSiB2 and GLASS simulations for different regions. The standard deviations of the SSiB4/TRIFFID simulation are closer to those of the GLASS simulation than to those of the SSiB2 simulation for different regions. The correlation coefficients between the GFS/SSiB2 and GIMMS/GLASS simulation are 0.58/0.57 (Fig. 3), respectively. The ratio of the total amount of bare land area in the global land area is larger in the GFS/SSiB2 simulation (about 65%) than in the other three simulations over high latitudes, South Asia, and the dry regions of Australia (Table 5), where they are only 52%, 42%, and 40% for the GFS/SSiB4/TRIFFID, GIMMS, and GLASS simulations, respectively.

Large seasonal changes in the LAI occur in the Northern Hemisphere in the satellite observations. Figures 3d$_1$–d$_4$ compare the spatial correlation coefficients for JJA − DJF. Although the correlations between the GFS/SSiB4/TRIFFID and GIMMS/GLASS simulations are 0.79/0.81, the correlation coefficients between the GFS/SSiB2 and GIMMS/GLASS simulations are only 0.60/0.65 (Fig. 3). The spatial correlation coefficients are statistically significant at the significance level of 0.01. The vegetation specified in the GFS/SSiB2 simulation is unable to catch the features simulated by the GFS/SSiB4/TRIFFID simulations. In addition, the latitudinal variations of the zonally averaged LAI in Figs. 4a–d also show that the GFS/SSiB4/TRIFFID simulation is closer

to the observations.

Figure 5 compares the temporal correlations between the monthly LAI in the SSiB2 simulation and the LAI in the GIMMS and GLASS simulations from 1982 to 2008. In the SSiB2 simulation, the LAI has a monthly but not an interannual variation. The LAI data are extended by repeating the 12 monthly values for each year for the entire period.

Figure 5 shows that the global spatial correlation between the GFS/SSiB4/TRIFFID LAI and the satellite-derived LAI is consistently higher than that between the GFS/SSiB2 LAI and the satellite-derived LAI in every year. The temporal correlation coefficients between the globally averaged monthly GFS/SSiB2 LAI and the GIMMS/GLASS LAI are only 0.31/0.29, respectively, although the correlation coefficients for the GFS/SSiB4/TRIFFID simulations are 0.47/0.46, respectively. The correlation coefficients increase by about 51% and 58%, respectively. The high correlations mainly occur in the Northern Hemisphere. The GFS/SSiB4/TRIFFID and GFS/SSiB2 simulations give similar results over the Amazon region, which is covered by dense evergreen forest with limited monthly variation, and the global dry arid regions with a small LAI.

Figure 6 shows the interannual variations in the spatial correlations of the global annual LAI between the simulations and GLASS and the root-mean-square error (RMSE). The correlation coefficient between the GIMMS and the GLASS data is about 0.95. The correlation coefficient between the LAI produced by the GFS/SSiB4/TRIFFID simulation and the GLASS data is about 0.57, which is closer to the observations than the
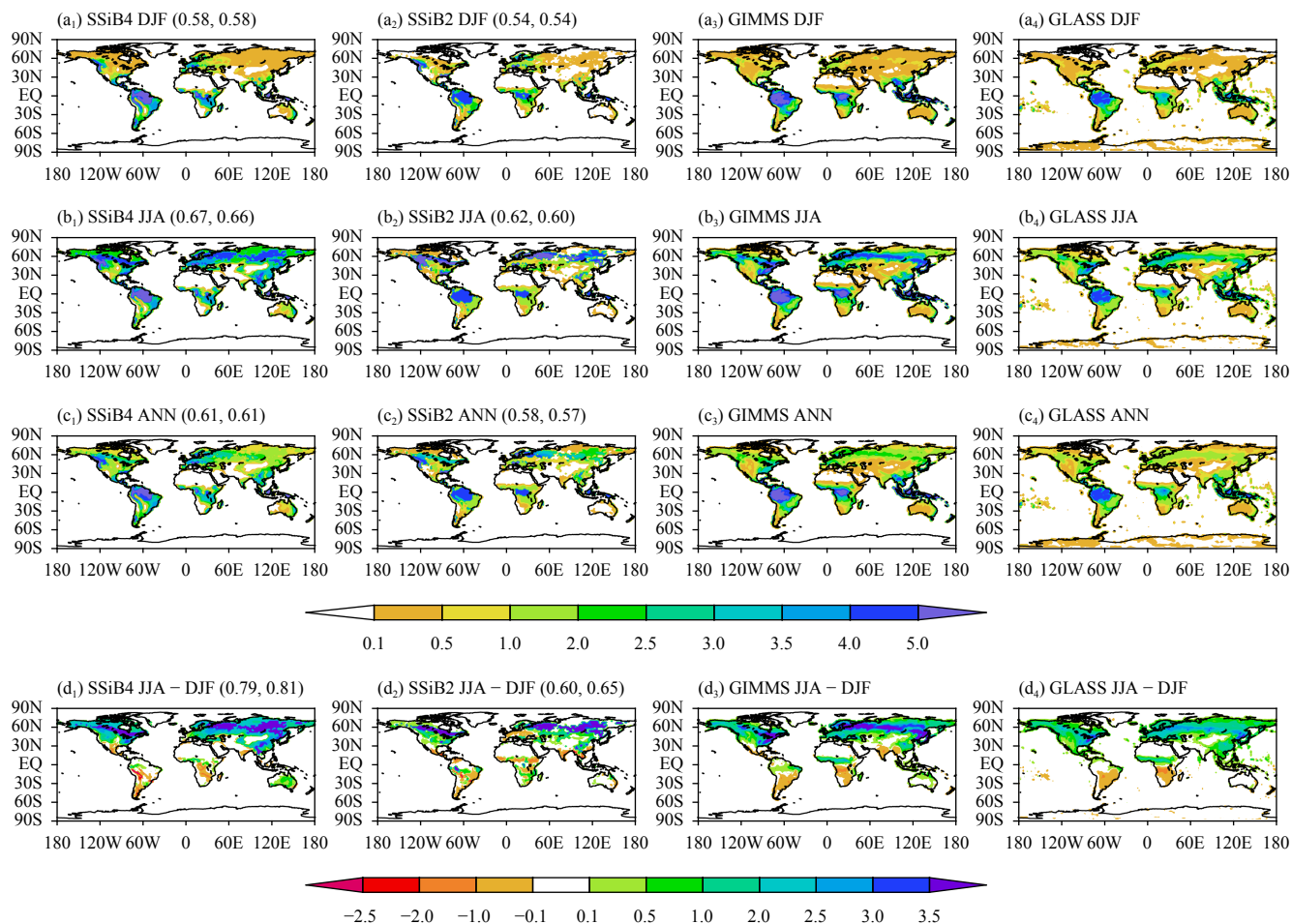
Fig. 3. Simulated and satellite-derived LAI averaged from 1982 to 2008. (a_1, b_1, c_1, d_1) GFS/SSiB4/TRIFFID simulation, (a_2, b_2, c_2, d_2) specified in GFS/SSiB2, (a_3, b_3, c_3, d_3) GIMMS, and (a_4, b_4, c_4, d_4) GLASS for DJF, JJA, annual average, and difference between summer and winter. The values in parentheses in the subtitle of each panel in two left-hand columns are the global spatial correlations between the simulated LAI and the GIMMS/GLASS LAI, respectively.

Table 4. Spatially averaged correlation coefficients between the simulated LAI by the SSiB4/TRIFFID (S4)/SSiB2 (S2) and GLASS LAI (G) simulations and the standard deviations from 1982 to 2002 for different regions

Region		1	2	3	4	5	6	7	8	Globe
Correlation coefficient	S4	0.32	0.20	0.17	0.78	0.50	0.20	0.64	0.06	0.46
	S2	0.11	0.08	0.15	0.53	0.46	−0.02	0.47	0.05	0.29
	G	0.33	0.30	0.58	0.72	0.52	0.48	0.80	0.19	0.45
Standard deviation	S4	0.22	0.17	0.23	0.68	0.21	0.28	0.84	0.25	0.19
	S2	0.13	0.09	0.15	0.56	0.15	0.20	0.55	0.08	0.13

Table 5. Comparisons of the amount of bare land area (%) between the simulations and observations (GIMMS and GLASS)

Season	GFS/SSiB4/TRIFFID		GFS/SSiB2		GIMMS		GLASS	
	DJF	JJA	DJF	JJA	DJF	JJA	DJF	JJA
Southeast Asia	75	75	76	77	48	48	34	33
Australia	66	58	86	86	37	37	31	32
30°–65°N	53	52	68	65	49	42	54	40

GFS/SSiB2 simulation. The spatial RMSE between the GFS/SSiB4/TRIFFID simulation and the satellite-derived LAI is consistently smaller than that for the GFS/SSiB2 simulation.
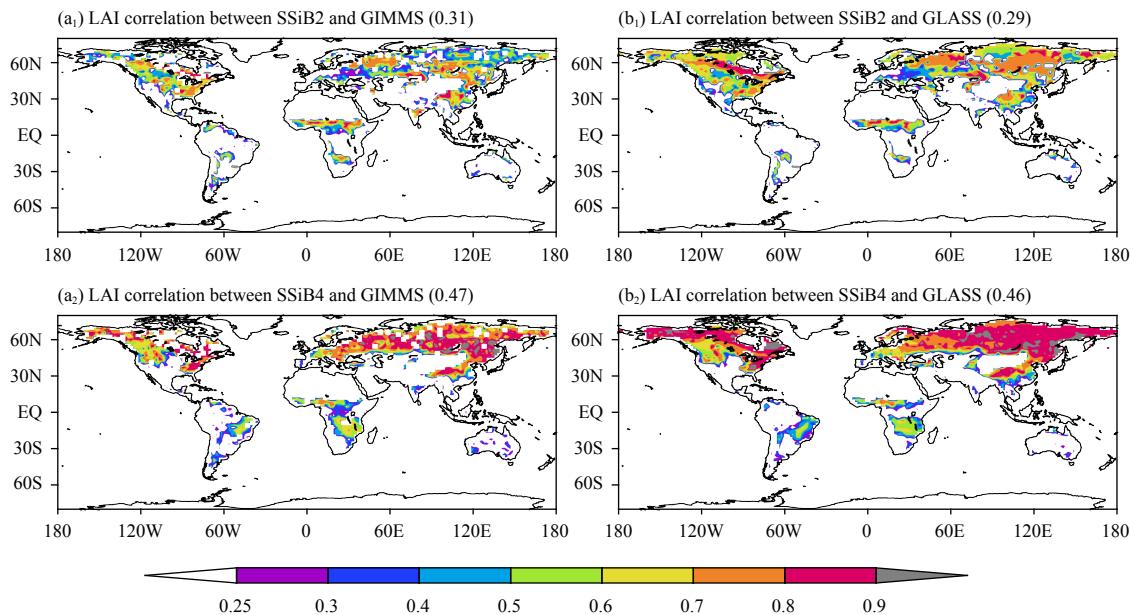
3.2   *Evaluation of the simulated surface albedo*

The change in the land surface albedo is highly correlated with the vegetation cover (Brovkin et al., 2013). Because there is an interannual variation in the vegetation
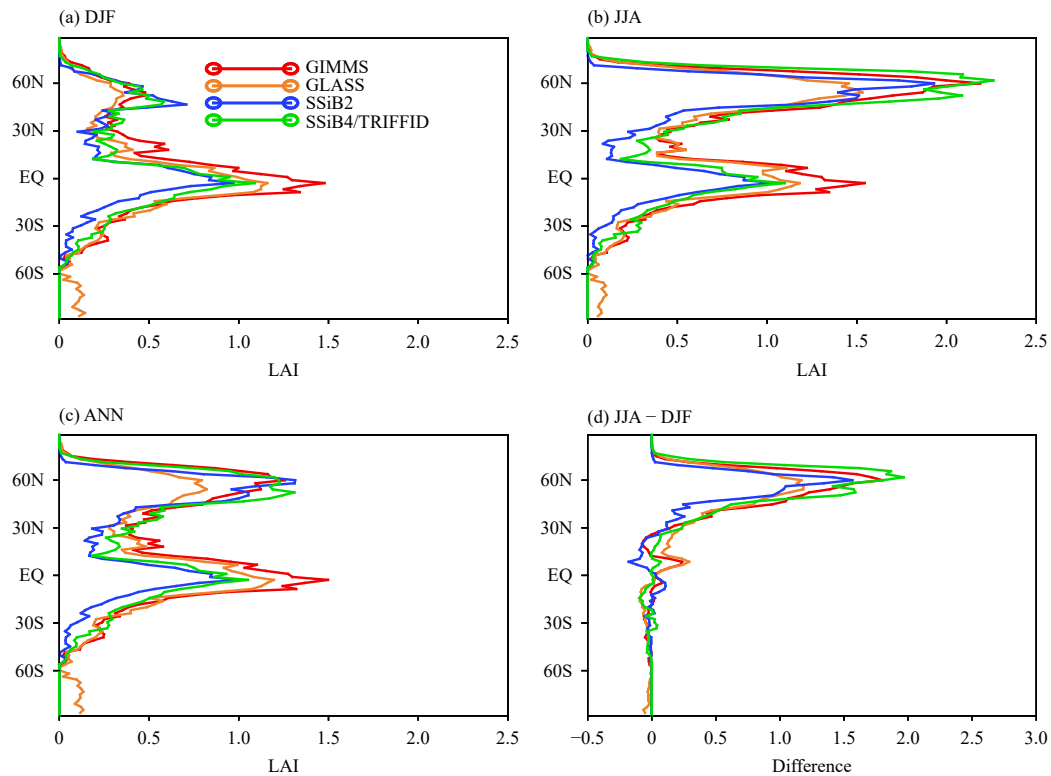
Fig. 4. Comparisons of the zonal mean JJA and DJF LAI between the simulations and satellite products averaged over the time period 1982–2008.


Fig. 5. Correlations of the monthly LAI between the SSiB2 and (a$_1$) GIMMS/(b$_1$) GLASS simulations and between the SSiB4/TRIFFID and (a$_2$) GIMMS/(b$_2$) GLASS simulations during the time period 1982–2008.

cover and other vegetation conditions on the land surface in the GFS/SSiB4/TRIFFID simulation, the surface albedo, roughness, and ground evaporation are also changed.

Figure 7 shows the correlations, RMSE, and the differ-

ences between the simulations and observations. The results are calculated based on monthly data at every grid point from 1982 to 2008. Figure 7 shows that the albedo produced by the GFS/SSiB4/TRIFFID and MODIS albedo have relatively high correlations compared with the
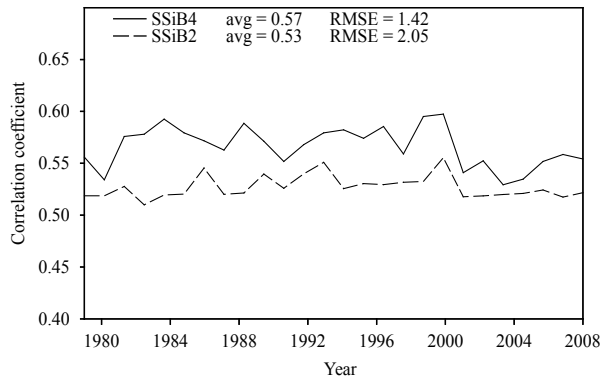
Fig. 6. Comparison of the spatial correlations between the simulated global annual LAI and the GLASS simulation.

GFS/SSiB2 albedo, especially at midlatitudes in the Northern Hemisphere, and a relatively low RMSE. The large RMSE between the albedo produced by the GFS/SSiB2 and the MODIS albedo occurs at high latitudes in the Northern Hemisphere, which may be attributed to the snow cover and snow-masking effects of trees.

Figure 7 shows that, in general, the correlation coefficient between the GFS/SSiB4/TRIFFID and MODIS albedo increases, but there are still some areas in which the coefficient decreases. The area with a large negative coefficient occurs in Australia, corresponding to a large RMSE. As seen from the statistics in Table 6, the simu-
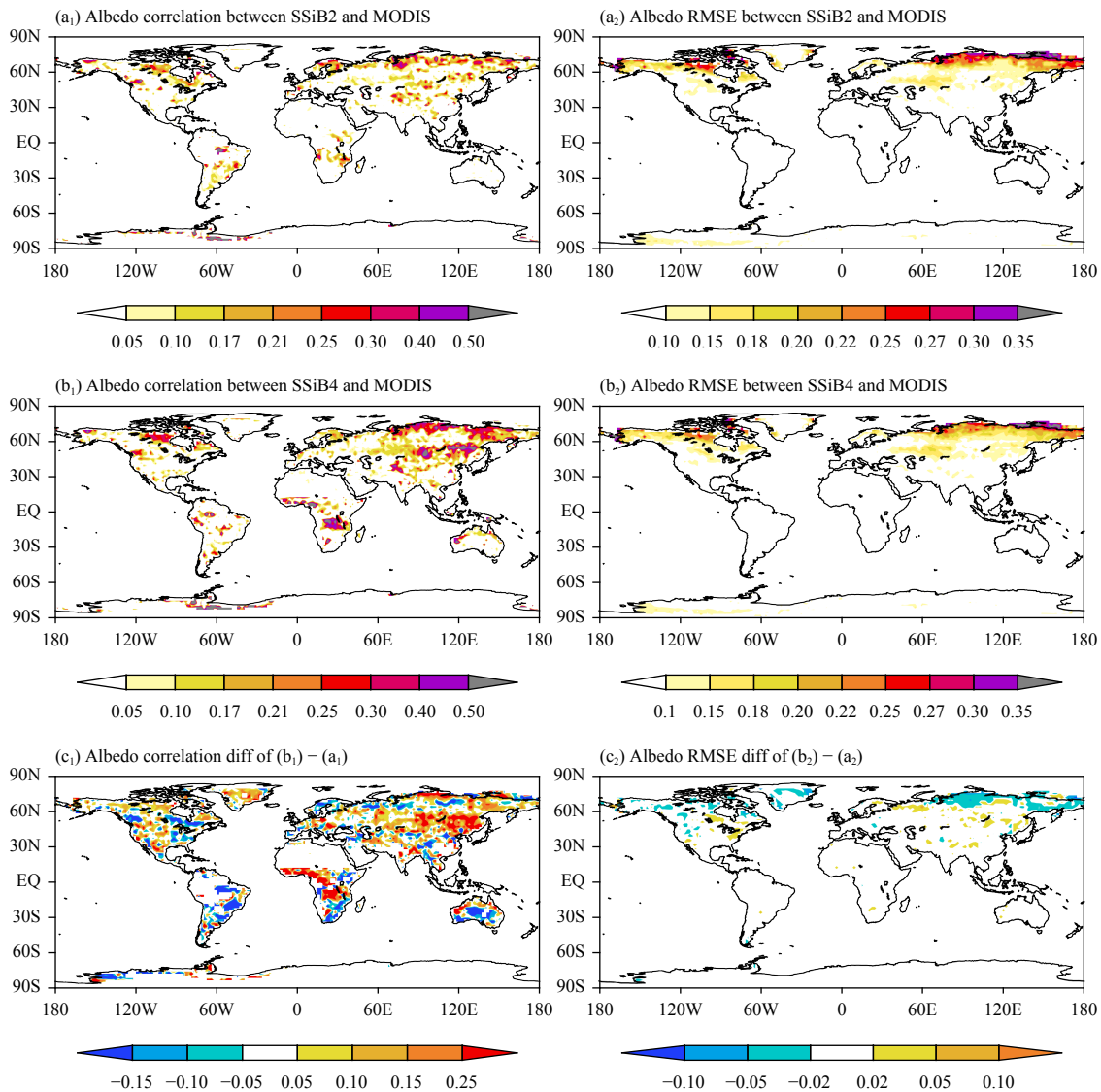
Fig. 7. Comparisons of (a_1) the correlations between the GFS/SSiB2 simulated monthly albedo from 1982 to 2008 and MODIS, (b_1) the correlations between the GFS/SSiB4/TRIFFID simulated monthly albedo and MODIS, and (c_1) the difference between (b_1) and (a_1). RMSE for (a_2) GFS/SSiB2, (b_2) GFS/SSiB4/TRIFFID, and (c_2) the difference between (b_2) and (a_2).

lated regional average albedo of the GFS/SSiB4/TRIF-FID simulation is lower by about 3% than that of the GFS/SSiB2 simulation, which may be caused by the overestimation of the LAI (Figs. 3a$_1$–d$_1$).

3.3 Assessing the simulated surface air temperature and precipitation

A more realistic LAI and albedo should produce better climate simulations. This section compares the simulated atmospheric results from the GFS/SSiB4/TRIFFID and GFS/SSiB2 simulations with the observations.

3.3.1 Correlation between simulated surface air temperature and CAMS temperature

To evaluate the relationship between the simulated near-surface air temperature and the observations, the correlations between the air temperature at 2 m above the ground simulated by the GFS/SSiB4/TRIFFID and GFS/SSiB2 models and the near-surface air temperature of GHCN_CAMS at 2 m were calculated (Fig. 8).

After including the dynamic vegetation processes, the correlation between the temperature modeled by the GFS/SSiB4/TRIFFID simulation and the temperature of GHCN_CAMS increases (Fig. 8c). Apart from the region near the equator, where in some areas, the correlation is reduced after considering the dynamic vegetation, the correlation increases in southern Africa, southern

Asia, and most of the midlatitudes of the Northern and Southern Hemispheres. These results suggest that incorporating dynamic vegetation processes in land surface models improves the modeling of surface temperature, especially over midlatitudes in both the Northern and Southern Hemispheres.

The temporal correlation between the simulated monthly surface air temperature and the GHCN_CAMS temperature is also calculated for the different sub-regions (as defined in Fig. 1) and the statistical results are listed in Table 6. The correlation coefficients in Table 6 are statistically significant at a significance level of 0.01, which shows the effects of the improvement in the dynamic vegetation processes on simulations of the surface air temperature, in particular in Africa, Southeast Asia, and South America. This will, in turn, improve the energy balance at the land surface.

3.3.2 Correlation between simulated precipitation and CMAP precipitation

Figure 9 shows the correlations between the monthly mean precipitation simulated by the coupled GFS/SSiB4/TRIFFID and GFS/SSiB2 models and the CMAP precipitation. The correlation is calculated by using monthly data from 1979 to 2008. Figure 9c shows the difference between the GFS/SSiB4/TRIFFID and GFS/SSiB2 simulations. In general, the incorporation of the dynamic ve-
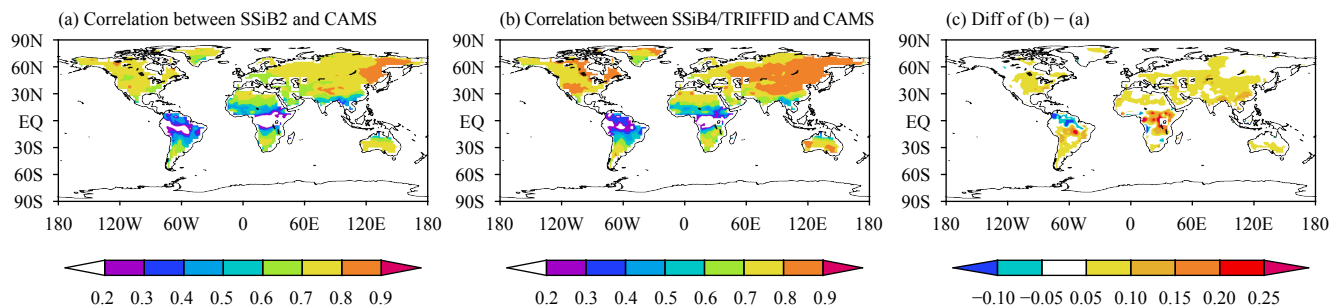
Fig. 8. Correlations between the CAMS monthly near-surface temperature (1979–2008) and (a) the GFS/SSiB2 simulation, (b) the GFS/SSiB4/TRIFFID simulation, and (c) the difference between (b) and (a).

Table 6. Comparison of the correlations between the simulated and CAMS monthly near-surface temperature (C1) and correlations between the simulated and CMAP monthly precipitation (C2) from 1979 to 2008, and the average differences in the surface variables between the SSiB4/TRIFFID and SSiB2 (D) simulations from 1982 to 2002 in different regions

Region		1	2	3	4	5	6	7	8	Globe
	SSiB2	0.50	0.65	0.35	0.77	0.68	0.39	0.72	0.68	0.60
C1	SSiB4/TRIFFID	0.56	0.72	0.41	0.82	0.70	0.44	0.77	0.72	0.66
	Increase (%)	12	11	17	7	3	13	7	6	10
	SSiB2	0.19	0.22	0.21	0.22	0.19	0.25	0.11	0.14	0.19
C2	SSiB4/TRIFFID	0.25	0.27	0.22	0.28	0.19	0.27	0.12	0.15	0.22
	Increase (%)	32	23	5	27	0	8	9	7	16
	Precipitation (mm day^{-1})	0.23	−0.08	−0.21	−0.10	0.04	−0.02	−0.10	0.31	0.01
	Latent heat flux (W m^{-2})	0.47	−0.71	−3.15	−1.76	0.84	0.83	−5.11	5.89	0.28
D	Sensible heat flux (W m^{-2})	−1.89	−0.85	0.64	−0.80	−0.55	−0.24	−1.36	1.69	−0.43
	Near-surface temperature (°C)	−0.30	−0.11	−0.23	−0.70	−0.21	−0.02	−0.72	0.52	−0.17
	Albedo (%)	0.29	0.13	0.10	0.85	0.22	0.35	2.39	−3.02	0.09
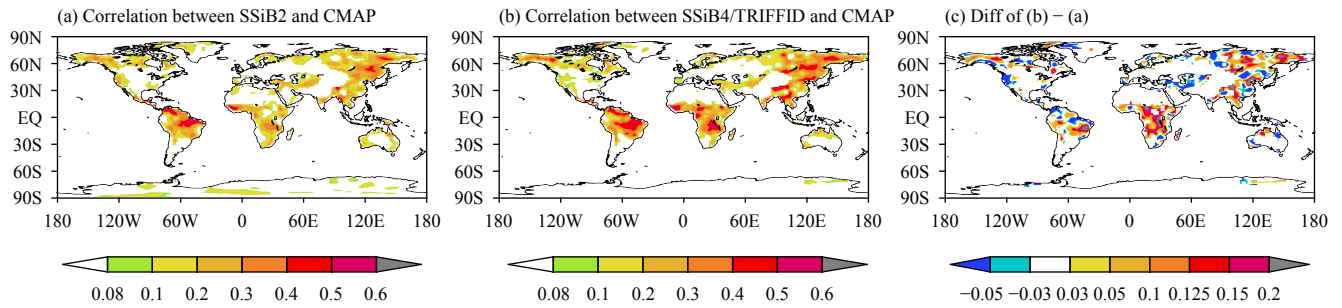
Fig. 9. Correlations between the CMAP monthly mean precipitation (1979–2008) and (a) the GFS/SSiB2 simulation, (b) the GFS/SSiB4/TRIFFID simulation, and (c) the difference between (b) and (a).

getation model into the land surface model improves the simulation of precipitation, but the results vary among different regions.

Table 6 lists the correlation for the monthly precipitation from 1979 to 2008 for the eight sub-regions and the whole globe. The correlation coefficients are lower than those for temperature, but are still statistically significant at the 0.01 significance level for different regions. There is a significant improvement in precipitation over Africa, eastern Asia, southern America, and Australia. The improved LAI and surface albedo contribute to these improvements.

The dynamic vegetation model better describes the seasonal and annual variation in vegetation. It has long been known that there is strong vegetation–precipitation feedback on both continental and global scales (Charney et al., 1977; Xue et al., 1990, 2010; Wang et al., 2004; Kucharski et al., 2013; Li et al., 2018). The results in Fig. 9 and Table 6 further demonstrate that including the dynamic vegetation processes can improve the correlation between the simulated and observation precipitation in the Sahel region.

3.4 Relationship between LAI and surface temperature

In the GFS/SSiB4/TRIFFID simulation, the parameters related to vegetation (e.g., the LAI and PFT fraction)

change with climate. The LAI in the SSiB4/TRIFFID simulation interacts with the climate, whereas the LAI in the SSiB2 simulation does not respond to climate variability. The temporal correlations between the surface temperature and the observed, specified, and simulated LAIs were analyzed by using the monthly mean data from 1982 to 2008 (Fig. 10). Figure 10 only shows the correlation coefficients that reach the statistically significant level of 0.01.

The correlation coefficient between the LAI and the temperature modeled by the GFS/SSiB4/TRIFFID simulation is significantly greater than that between the specified LAI and the temperature modeled by the GFS/SSiB2 simulation and is more consistent with the correlations between the GLASS LAI and the GHCN_CAMS temperatures. A positive correlation mainly occurs in the high latitudes of the Northern Hemisphere, whereas a negative correlation mainly appears at low latitudes near the equator. This result is in agreement with the general consensus that the positive correlation at high latitudes results from both warming enhancing the growth of vegetation and more vegetation (and therefore a lower albedo) favoring warming. In the tropics, the negative correlation results from the heat stress on vegetation and the cooling effect of vegetation through evaporative cooling.
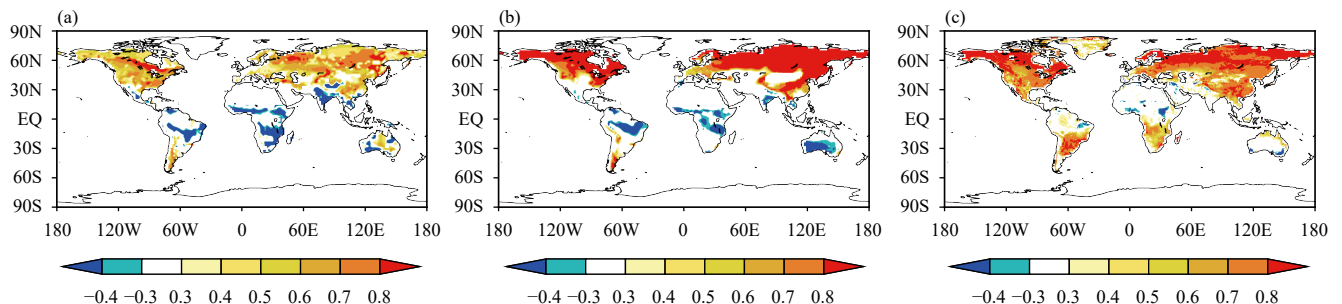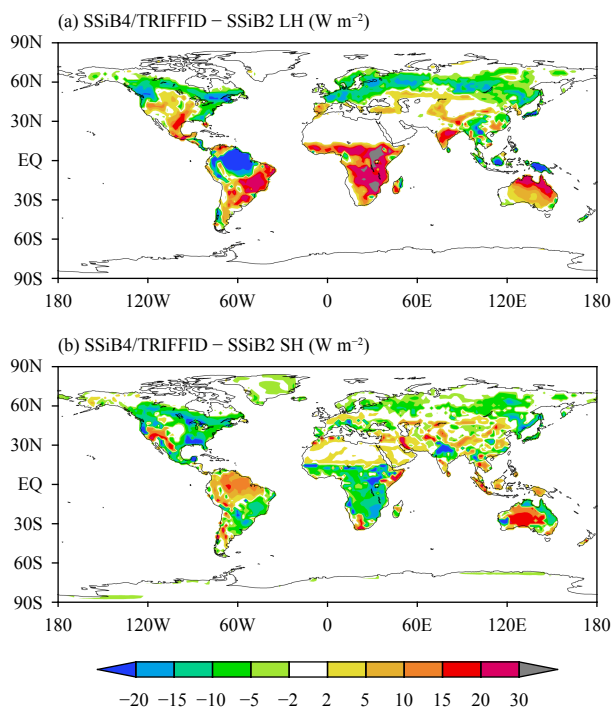

Fig. 10. Correlations for the time period 1982–2008 (a) between the monthly surface temperature simulated by the GFS/SSiB2 and GFS/SSiB2 LAI models, (b) between the monthly surface temperature simulated by the GFS/SSiB4/TRIFFID and GFS/SSiB4/TRIFFID LAI models, and (c) between the monthly GLASS LAI and CAMS temperature.

4.   Water and energy budgets

Land surface processes modulate the surface water and energy cycles, which in turn, affect the atmospheric circulation. Changes in the surface energy and water balance result in different results for the simulation of precipitation and surface temperature by the GFS/SSiB4/TRIFFID and GFS/SSiB2 models.

Figures 11a and 11b show the average difference in the simulated surface latent and sensible heat fluxes between the GFS/SSiB4/TRIFFID and GFS/SSiB2 models from 1979 to 2008, respectively. In most parts of the world (e.g., Africa, South America, and Australia), the signs of the difference in sensible heat flux are the opposite to those of the difference in the latent heat flux. In these areas, there is no large difference in the albedo and, in turn, the net radiation, between these two runs (Fig. 7). The dynamic vegetation processes therefore just produce a different energy partitioning from the SSiB2 model. However, in many other regions (e.g., areas of boreal forest at mid and high latitudes in the Northern Hemisphere), where the albedo shows substantial differences (Fig. 7), the changes in both the sensible and latent heat flux have a positive sign, suggesting an increase in net radiation as a result of the difference in the albedo. Table 6 summarizes the changes in the surface energy components.

Figure 12 shows the difference between the precipitation modeled by GFS/SSiB4/TRIFFID and GFS/SSiB2 averaged over the time period 1979–2008. The largest increase in precipitation appears over southern Africa, Australia, large parts of South America, and the Great Plains of North America. By contrast, precipitation decreases over the mid to high latitudes of the Northern Hemisphere and Southeast Asia. A comparison of Figs. 12 and 11a shows that the positive and negative patterns are very similar, suggesting that the change in the latent heat flux has a dominant role in precipitation. This similarity also reflects the effect of water limitation on the latent heat flux.

Modulation of the surface energy balance by the vegetation dynamics contributes to the difference in precipitation. A comparison with Figs. 5, 7, and 9 shows that most of the areas with a large difference in precipitation in Fig. 12 are coincident with the areas with an increased correlation coefficient between the simulated and observed precipitation (Fig. 9), as well as the simulated and observed LAI/albedo (Fig. 5/Fig. 7). The inclusion of dynamic vegetation produces more consistent and realistic surface conditions, which should contribute to a more realistic simulation of precipitation.

5.   Conclusions and discussion

This study used two general circulation models (1) the NCEP GFS coupled with the biophysical model SSiB2 and (2) the NCEP GFS coupled with the biophysical and dynamic vegetation models SSiB4/TRIFFID to investigate the effects of dynamic vegetation processes on numerical climate simulations. Two experiments were conducted globally by integrating the GFS/SSiB2 and GFS/SSiB4/TRIFFID simulations from 1948 to 2008. By

Fig. 11. Mean difference in the simulated land surface (a) latent heat (LH) flux and (b) sensible heat (SH) flux between the GFS/SSiB4/TRIFFID and GFS/SSiB2 simulations.
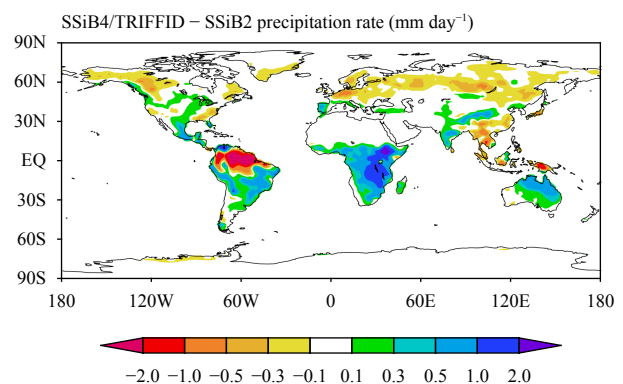
Fig. 12. Mean difference in precipitation between the GFS/SSiB4/TRIFFID and GFS/SSiB2 simulations.

comparing the results from these two runs and observational datasets, the effects of dynamic vegetation processes on the simulation of climate and its variability were delineated.

The temporal correlation between the globally averaged monthly LAI modeled by the NCEP GFS/SSiB4/TRIFFID simulation and the satellite-derived LAI increased by > 50% compared with the GFS/SSiB2 simulation; for JJA and DJF, it increased by about 32% and 25%, respectively. The correlation coefficients between the GFS/SSiB4/TRIFFID simulated LAI/surface albedo and the satellite-derived LAI/albedo were significantly higher than those of the GFS/SSiB2 simulation, which specifies vegetation conditions based on a table. This suggests that the land surface model including dynamic vegetation processes can more realistically present land surface processes and the surface energy balance and has the potential to provide better land–atmosphere interactions and climate simulations.

Our main conclusions are summarized as follows.

(1) After incorporation of the dynamic vegetation processes, the interannual variation of vegetation cover can be better simulated over many parts of the world, especially in semiarid regions where the climate is sensitive to vegetation conditions.

(2) The near-surface temperature is better simulated when using improved simulations in the surface variables and associated surface energy balance. The correlations between the simulated and observed monthly mean near-surface air temperature over Africa, Southeast Asia, and South America increased by about 13%, 17%, and 16%, respectively.

(3) Dynamic vegetation processes can effectively modulate local changes in precipitation, which are consistent with the spatial patterns of changes in the surface latent heat flux, suggesting that the evaporation is the dominant factor in influencing the seasonal and interannual variation of precipitation.

REFERENCES

Bartholomé, E., and A. S. Belward, 2005: GLC2000: a new approach to global land cover mapping from Earth observation data. *Int. J. Remote Sens.*, **26**, 1959–1977, doi: 10.1080/01431160412331291297.

Brovkin, V., L. Boysen, T. Raddatz, et al., 2013: Evaluation of vegetation cover and land-surface albedo in MPI-ESM CMIP5 simulations. *J. Adv. Model. Earth Syst.*, **5**, 48–57, doi: 10.1029/2012MS000169.

Cao, X. M., X. Chen, A. M. Bao, et al., 2011: Response of vegetation to temperature and precipitation in Xinjiang during the period of 1998–2009. *J. Arid Land*, **3**, 94–103, doi: 10.3724/SP.J.1227.2011.00094.

Charney, J., W. J. Quirk, S. H. Chow, et al., 1977: A comparative study of the effects of albedo change on drought in semi-arid regions. *J. Atmos. Sci.*, **34**, 1366–1385, doi: 10.1175/1520-0469(1977)034<1366:ACSOTE>2.0.CO;2.

Claussen, M., S. Bathiany, V. Brovkin, et al., 2013: Simulated climate–vegetation interaction in semi-arid regions affected by plant diversity. *Nat. Geosci.*, **6**, 954–958, doi: 10.1038/ngeo1962.

Cox, P. M., 2001: Description of the "TRIFFID" Dynamic Global Vegetation Model. Hadley Centre Technical Note 24, Met Office, London Road, Bracknell, 16 pp.

Cox, P. M., R. A. Betts, C. D. Jones, et al., 2000: Acceleration of global warming due to carbon-cycle feedbacks in a coupled climate model. *Nature*, **408**, 184–187, doi: 10.1038/35041539.

Crucifix, M., R. A. Betts, and P. M. Cox, 2005: Vegetation and climate variability: a GCM modelling study. *Climate Dyn.*, **24**, 457–467, doi: 10.1007/s00382-004-0504-z.

DeFries, R. S., and J. R. G. Townshend, 1994: NDVI-derived land cover classifications at a global scale. *Int. J. Remote Sens.*, **15**, 3567–3586, doi: 10.1080/01431169408954345.

Delire, C., J. A. Foley, and S. Thompson, 2004: Long-term variability in a coupled atmosphere–biosphere model. *J. Climate*, **17**, 3947–3959, doi: 10.1175/1520-0442(2004)017<3947:LVIACA>2.0.CO;2.

Delire, C., N. de Noblet-Ducoudré, A. Sima, et al., 2011: Vegetation dynamics enhancing long-term climate variability confirmed by two models. *J. Climate*, **24**, 2238–2257, doi: 10.1175/2010JCLI3664.1.

Fan, Y., and H. van den Dool, 2008: A global monthly land surface air temperature analysis for 1948–present. *J. Geophys. Res. Atmos.*, **113**, D01103, doi: 10.1029/2007JD008470.

Gao, F., C. B. Schaaf, A. H. Strahler, et al., 2005: MODIS bidirectional reflectance distribution function and albedo Climate Modeling Grid products and the variability of albedo for major global vegetation types. *J. Geophys. Res. Atmos.*, **110**, D01104, doi: 10.1029/2004JD005190.

Harper, A. B., P. M. Cox, P. Friedlingstein, et al., 2016: Improved representation of plant functional types and physiology in the Joint UK Land Environment Simulator (JULES v4.2) using plant trait information. *Geosci. Model Dev.*, **9**, 2415–2440, doi: 10.5194/gmd-9-2415-2016.

He, T., S. L. Liang, and D.-X. Song, 2014: Analysis of global land surface albedo climatology and spatial-temporal variation during 1981–2010 from multiple satellite products. *J. Geophys. Res. Atmos.*, **119**, 10,281–10,298, doi: 10.1002/2014JD021667.

Kucharski, F., N. Zeng, and E. Kalnay, 2013: A further assess-

ment of vegetation feedback on decadal Sahel rainfall variability. *Climate Dyn.*, **40**, 1453–1466, doi: 10.1007/s00382-012-1397-x.

Latifovic, R., Z. L. Zhu, J. Cihlar, et al., 2002: Land Cover of North America 2000. Natural Resources Canada, Canada Center for Remote Sensing, US Geological Service EROS Data Center, Sioux Falls, South Dakota.

Levis, S., and G. B. Bonan, 2004: Simulating springtime temperature patterns in the Community Atmosphere Model coupled to the Community Land Model using prognostic leaf area. *J. Climate*, **17**, 4531–4540, doi: 10.1175/3218.1.

Li, Y., E. Kalnay, S. Motesharrei, et al., 2018: Climate model shows large-scale wind and solar farms in the Sahara increase rain and vegetation. *Science*, **361**, 1019–1022, doi: 10.1126/science.aar5629.

Liu, Y., and Y. K. Xue, 2020: Expansion of the Sahara Desert and shrinking of frozen land of the Arctic. *Sci. Rep.*, **10**, 4109, doi: 10.1038/s41598-020-61085-0.

Liu, Y., Y. K. Xue, G. MacDonald, et al., 2019: Global vegetation variability and its response to elevated CO_2, global warming, and climate variability—a study using the offline SSiB4/TRIFFID model and satellite data. *Earth Syst. Dyn.*, **10**, 9–29, doi: 10.5194/esd-10-9-2019.

Lucht, W., C. B. Schaaf, and A. H. Strahler, 2000: An algorithm for the retrieval of albedo from space using semiempirical BRDF models. *IEEE Trans. Geosci. Remote Sens.*, **38**, 977–998, doi: 10.1109/36.841980.

MacDonald, G. M., 2010: Water, climate change, and sustainability in the southwest. *Proc. Natl. Acad. Sci. USA*, **107**, 21,256–21,262, doi: 10.1073/pnas.0909651107.

Mayaux, P., E. Bartholomé, S. Fritz, et al., 2004: A new land-cover map of Africa for the year 2000. *J. Biogeogr.*, **31**, 861–877, doi: 10.1111/j.1365-2699.2004.01073.x.

Pinzon, J., M. E. Brown, and C. J. Tucker, 2005: Satellite time series correction of orbital drift artifacts using empirical mode decomposition. *Hilbert-Huang Transform: Introduction and Applications*, N. Huang, Ed., World Scientific, Singapore, 167–186.

Qiu, B., W. D. Guo, Y. K. Xue, et al., 2016: Implementation and evaluation of a generalized radiative transfer scheme within canopy in the soil-vegetation-atmosphere transfer (SVAT) model. *J. Geophys. Res. Atmos.*, **121**, 12,145–12,163, doi: 10.1002/2016JD025328.

Schaaf, C. B., F. Gao, A. H. Strahler, et al., 2002: First operational BRDF, albedo nadir reflectance products from MODIS. *Remote Sens. Environ.*, **83**, 135–148, doi: 10.1016/S0034-4257(02)00091-3.

Sellers, P. J., C. J. Tucker, G. J. Collatz, et al., 1996: A revised land surface parameterization (SiB2) for atmospheric GCMs. Part II: The generation of global fields of terrestrial biophysical parameters from satellite data. *J. Climate*, **9**, 706–737, doi: 10.1175/1520-0442(1996)009<0706:ARLSPF>2.0.CO;2.

Shi, Y., M. Yu, A. Erfanian, et al., 2018: Modeling the dynamic vegetation–climate system over China using a coupled regional model. *J. Climate*, **31**, 6027–6049, doi: 10.1175/JCLI-D-17-0191.1.

Wang, G., E. A. B. Eltahir, J. A. Foley, et al., 2004: Decadal variability of rainfall in the Sahel: results from the coupled GENESIS-IBIS atmosphere-biosphere model. *Climate Dyn.*, **22**, 625–637, doi: 10.1007/s00382-004-0411-3.

Wang, G. L., S. S. Sun, and R. Mei, 2011: Vegetation dynamics contributes to the multi-decadal variability of precipitation in the Amazon region. *Geophys. Res. Lett.*, **38**, L19703, doi: 10.1029/2011GL049017.

Wang, Y., M. Notaro, Z. Liu, et al., 2008: Detecting vegetation-precipitation feedbacks in mid-Holocene North Africa from two climate models. *Clim. Past*, **4**, 59–67, doi: 10.5194/cp-4-59-2008.

Woodward, F. I., M. R. Lomas, and C. K. Kelly, 2004: Global climate and the distribution of plant biomes. *Philos. Trans. Roy. Soc. B Biol. Sci.*, **359**, 1465–1476, doi: 10.1098/rstb.2004.1525.

Wu, M. C., G. Schurgers, M. Rummukainen, et al., 2016: Vegetation–climate feedbacks modulate rainfall patterns in Africa under future climate change. *Earth Syst. Dyn.*, **7**, 627–647, doi: 10.5194/esd-7-627-2016.

Xiao, Z. Q., S. L. Liang, J. D. Wang, et al., 2016: Long-time-series Global Land Surface Satellite leaf area index product derived from MODIS and AVHRR surface reflectance. *IEEE Trans. Geosci. Remote Sens.*, **54**, 5301–5318, doi: 10.1109/TGRS.2016.2560522.

Xie, P. P., and P. A. Arkin, 1997: Global precipitation: A 17-year monthly analysis based on gauge observations, satellite estimates, and numerical model outputs. *Bull. Amer. Meteor. Soc.*, **78**, 2539–2558, doi: 10.1175/1520-0477(1997)078<2539:GPAYMA>2.0.CO;2.

Xue, Y., P. J. Sellers, J. L. Kinter, et al., 1991: A simplified biosphere model for global climate studies. *J. Climate*, **4**, 345–364, doi: 10.1175/1520-0442(1991)004<0345:ASBMFG>2.0.CO;2.

Xue, Y., F. J. Zeng, K. E. Mitchell, et al., 2001: The impact of land surface processes on simulations of the U.S. hydrological cycle: A case study of the 1993 flood using the SSiB land surface model in the NCEP Eta regional model. *Mon. Wea. Rev.*, **129**, 2833–2860, doi: 10.1175/1520-0493(2001)129<2833:TIOLSP>2.0.CO;2.

Xue, Y. K., 2006: Interactions and feedbacks between climate and dryland vegetations. *Dryland Ecohydrology*, P. D'Odorico, A. Porporato, and C. W. Runyan, Eds., Springer, Cham, 139–169, doi: 10.1007/978-3-030-23269-6_7.

Xue, Y. K., K.-N. Liou, and A. Kasahara, 1990: Investigation of biogeophysical feedback on the African climate using a two-dimensional model. *J. Climate*, **3**, 337–352, doi: 10.1175/1520-0442(1990)003<0337:IOBFOT>2.0.CO;2.

Xue, Y. K., M. J. Fennessy, and P. J. Sellers, 1996: Impact of vegetation properties on U.S. summer weather prediction. *J. Geophys. Res. Atmos.*, **101**, 7419–7430, doi: 10.1029/95JD02169.

Xue, Y. K., H.-M. H. Juang, W.-P. Li, et al., 2004: Role of land surface processes in monsoon development: East Asia and West Africa. *J. Geophys. Res. Atmos.*, **109**, D03105, doi: 10.1029/2003JD003556.

Xue, Y. K., F. De Sales, R. Vasic, et al., 2010: Global and seasonal assessment of interactions between climate and vegetation biophysical processes: A GCM study with different land–vegetation representations. *J. Climate*, **23**, 1411–1433, doi: 10.1175/2009JCLI3054.1.

Yu, M., G. L. Wang, and J. S. Pal, 2016: Effects of vegetation

feedback on future climate change over West Africa. *Climate Dyn.*, **46**, 3669–3688, doi: 10.1007/s00382-015-2795-7.

Zeng, N., J. D. Neelin, K.-M. Lau, et al., 1999: Enhancement of interdecadal climate variability in the Sahel by vegetation interaction. *Science*, **286**, 1537–1540, doi: 10.1126/science.286. 5444.1537.

Zeng, X. D., X. B. Zeng, and M. Barlage, 2008: Growing temperate shrubs over arid and semiarid regions in the Community Land Model–Dynamic Global Vegetation Model. *Global Biogeochem. Cycl.*, **22**, GB3003, doi: 10.1029/2007GB003014.

Zeng, Z. Z., S. L. Piao, L. Z. X. Li, et al., 2017: Climate mitigation from vegetation biophysical feedbacks during the past three decades. *Nat. Climate Change*, **7**, 432–436, doi: 10. 1038/nclimate3299.

Zhan, X. W., Y. K. Xue, and G. J. Collatz, 2003: An analytical approach for estimating CO_2 and heat fluxes over the Amazonian region. *Ecol. Modelling*, **162**, 97–117, doi: 10.1016/S0304-3800(02)00405-2.

Zhang, X. T., S. L. Liang, K. C. Wang, et al., 2010: Analysis of global land surface shortwave broadband albedo from multiple data sources. *IEEE J. Sel. Top. Appl. Earth Obs. Remote Sens.*, **3**, 296–305, doi: 10.1109/JSTARS.2010.2049342.

Zhang, Z. Q., Y. K. Xue, G. MacDonald, et al., 2015: Investigation of North American vegetation variability under recent climate: A study using the SSiB4/TRIFFID biophysical/dynamic vegetation model. *J. Geophys. Res. Atmos.*, **120**, 1300–1321, doi: 10.1002/2014JD021963.

Zhi, H., P. X. Wang, L. Dan, et al., 2009: Climate-vegetation interannual variability in a coupled atmosphere-ocean-land model. *Adv. Atmos. Sci.*, **26**, 599–612, doi: 10.1007/s00376-009-0599-6.

Zhong, L., Y. M. Ma, M. S. Salama, et al., 2010: Assessment of vegetation dynamics and their response to variations in precipitation and temperature in the Tibetan Plateau. *Climatic Change*, **103**, 519–535, doi: 10.1007/s10584-009-9787-8.

Zhu, Z. C., J. Bi, Y. Z. Pan, et al., 2013: Global data sets of vegetation Leaf Area Index (LAI)3g and Fraction of Photosynthetically Active Radiation (FPAR)3g derived from Global Inventory Modeling and Mapping Studies (GIMMS) Normalized Difference Vegetation Index (NDVI3g) for the period 1981 to 2011. *Remote Sens.*, **5**, 927–948, doi: 10.3390/rs5020927.

Tech & Copy Editor: Qi WANG